ISSN 0020-4412, Instruments and Experimental Techniques, 2018, Vol. 61, No. 3, pp. 332–348. © Pleiades Publishing, Ltd., 2018.
Original Russian Text ©J. Adamczewski-Musch, P.G. Akishin, K.-H. Becker, S.G. Belogurov, J. Bendarouach, N.I. Boldyreva, C. Deveaux, V.V. Dobyrn, M. Dürr, J. Eschke, J. Förtsch, J. Heep, C. Höhne, K.-H. Kampert, A.V. Khanzadeev, L.M. Kochenda, J. Kopfer, P.A. Kravtsov, I. Kres, S.A. Lebedev, E.I. Lebedeva, E.N. Leonova, S.V. Linev, T. Mahmoud, W. Niebur, E.V. Ovcharenko, V. Patel, C. Pauly, M. Penschuck, D. Pfeifer, S. Querchfeld, J. Rautenberg, S. Reinecke, Yu.G. Riabov, E.V. Roshchin, V.M. Samsonov, V.N. Schetinin, O.P. Tarasenkova, M. Traxler, C. Ugur, M.E. Vznuzdaev, 2018, published in Pribory i Tekhnika Eksperimenta, 2018, No. 3, pp. 15–33.

APPLICATION OF COMPUTERS IN EXPERIMENTS

Development of the Readout and Data-Acquisition System for the RICH Detector of the CBM Experiment

J. Adamczewski-Musch[a], P. G. Akishin[b], K.-H. Becker[c], S. G. Belogurov[b, d], J. Bendarouach[e], N. I. Boldyreva[f], C. Deveaux[e], V. V. Dobyrn[f], M. Dürr[e], J. Eschke[a], J. Förtsch[c], J. Heep[e], C. Höhne[e], K.-H. Kampert[c], A. V. Khanzadeev[f, d], L. M. Kochenda[f, d], J. Kopfer[c, e], P. A. Kravtsov[f, d], I. Kres[c], S. A. Lebedev[e, b], E. I. Lebedeva[e], E. N. Leonova[f], S. V. Linev[a], T. Mahmoud[e], W. Niebur[a], E. V. Ovcharenko[b, *], V. Patel[c], C. Pauly[c], M. Penschuck[g], D. Pfeifer[c], S. Querchfeld[c], J. Rautenberg[c], S. Reinecke[c], Yu. G. Riabov[f], E. V. Roshchin[f, d], V. M. Samsonov[f, d], V. N. Schetinin[b, h], O. P. Tarasenkova[f], M. Traxler[a], C. Ugur[a], and M. E. Vznuzdaev[f]

[a] *GSI Helmholtz Zentrum für Schwerionen Forschung GmbH, Darmstadt, D-64291 Germany*
[b] *Joint Institute for Nuclear Research, Laboratory of Information Technologies, Dubna, 141980 Russia*
[c] *Department of Physics, Wuppertal University, Wuppertal, D-42097 Germany*
[d] *National Research Nuclear University, Moscow Engineering Physics Institute, Moscow, 115409 Russia*
[e] *Institute of Physics II and Institute of Applied Physics, Justus Liebig University Giessen, Giessen, D-35392 Germany*
[f] *Konstantinov Petersburg Nuclear Physics Institute, National Research Center Kurchatov Institute, Gatchina, 188300 Russia*
[g] *Institut für Kernphysik, Göthe University Frankfurt, Frankfurt am Main, D-60438 Germany*
[h] *Bauman Moscow State Technical University, Moscow, 105005 Russia*
**e-mail: eovchar@jinr.ru*

Received April 5, 2017; in final form, August 7, 2017

Abstract—A 64-channel readout and data-acquisition module is described in detail. It consists of an H12700 multianode photomultiplier tube, four PADIWA preamplifier boards, and a TRB v3 card that perform the functions of a time-to-digital converter and a data concentrator. The software modules that are necessary for operation of the prototype are described. The inter-channel delays are calibrated. The drift of individual delays does not exceed 0.5 ns for the entire measurement time. The spectra of the "time over threshold" (ToT) are investigated. The influence of periodic noise pickups and the need to improve circuit designs are revealed. The timing properties of the wavelength shifter and its effect on the detection efficiency for Cherenkov rings are investigated. The most intense component is characterized by a decay time of 1.1 ns and there are components with characteristic times of 3.8 and 45 ns. The influence of single-electron spectrum features on the detection efficiency for photoelectrons and the probability of false hits are determined. The total time resolution of 131 channels is 1.1 ns (FWHM). The results make it possible to use the investigated system of readout and data acquisition in the CBM experiment. Nevertheless, the elimination of the revealed shortcomings will provide the efficiency margin and improve the reliability of the system during long-term operation.

DOI: 10.1134/S0020441218030028

1. INTRODUCTION

The FAIR (Facility for Antiproton and Ion Research) accelerator facility [1] and, in particular, the CBM (Compressed Baryonic Matter) experimental setup [2–5], are currently under construction in Darmstadt, Germany. The physical program of the CBM experiment is aimed at studying the phase diagram of strongly interacting matter and the equation of state of matter at extremely high densities of baryonic matter, which are obtained in collisions of relativistic nuclei in an experiment with a fixed target.

The yields and distributions in the phase space of particles generated in the interaction region must be measured for the implementation of the program. For this purpose, in each event, it necessary that:

- short-lived particles, including very rare ones, be reconstructed by their decay products;
- long-lived products of interactions be identified;
- the centrality of the collision be measured (the impact parameter be determined);
- the reaction plane be determined.

To be capable of performing various measurements, the CBM setup will function in two configura-

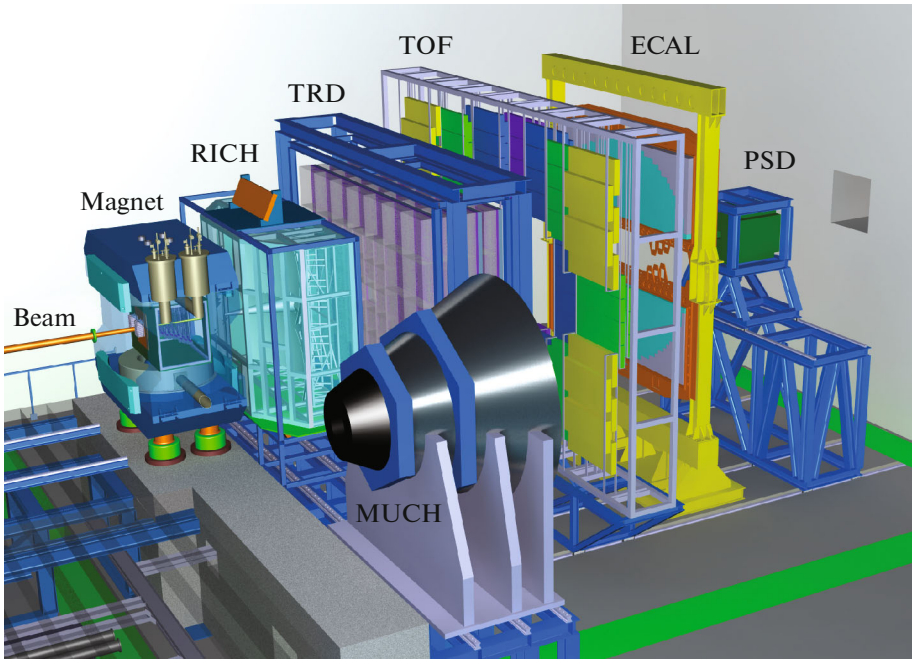

Fig. 1. The general view of the CBM experimental setup in the configuration with the RICH detector of Cherenkov rings: (MUCH) muon detector, (TRD) transient radiation detector, (TOF) time-of-flight detector, (ECAL) electromagnetic calorimeter, and (PSD) detector of non-interacting nuclear fragments.

tions: with the MUCH (Muon Chamber) muon detector and the RICH (Ring Image Cherenkov) detector of Cherenkov rings.

The diagram of the CBM experimental setup with the RICH detector is shown in Fig. 1.

Between the poles of the superconducting dipole magnet [6] is a vacuum chamber containing a target and the Micro Vertex Detector (MVD) [7]. The MVD is based on a monolithic pixel detector of the MAPS (Monolithic Active Pixel Sensor) type. Downstream of the beam, also between the poles, but, in contrast, outside the vacuum chamber, are the stations of the Silicon Tracking System (STS) [8], which are assembled from double-sided microstrip sensors. The MVD and STS coordinate tracking detectors have been designed to reconstruct trajectories of charged particles, to restore their momenta with an accuracy of at least 1%, and finding secondary vertices under conditions of high multiplicity and density of particles.

Next to the STS is the RICH detector of Cherenkov rings [9]. The RICH detector has been designed to identify electrons and positrons in a momentum range of 0.5–8.0 GeV/c in order to reconstruct decays of light vector mesons and J/ψ particles. This detector, whose development is discussed in this paper, has a 1.7-m-long radiator filled with carbon dioxide under a slight excess pressure and a focusing system of segmented spherical mirrors with a radius of 3 m and a total area of 13 m^2. A Hamamatsu H12700 multianode photomultiplier tube (MAPMT) is used as a position-sensitive photodetector.

In the alternative configuration the RICH detector is replaced with the MUCH muon system [10]. MUCH is intended primarily to study particles that undergo dimuon decay; it consists of alternating layers of iron and gas track chambers [11].

The transition radiation detector (TRD) is used to reconstruct particle tracks and identify electrons or positrons under conditions of a dominant pion background [12].

Hadrons are identified using a time-of-flight (TOF) detector [13].

The electromagnetic calorimeter (ECAL) of the "shashlyk" type is needed for detecting direct photons and photons from the decay of neutral mesons (π^0, η) [14].

The Projectile Spectator Detector (PSD) of noninteracting nuclear fragments [15] is a segmented hadron calorimeter that embraces small polar angles and serves to determine the impact parameter of a collision and the reaction plane.

The experiment is characterized by a high multiplicity of secondary particles, a large density of tracks at small angles, and a high frequency of interactions. As a result, the detectors contain tens of thousands of tightly packed readout channels operating without a triggering system, from which a large data stream must be collected and analyzed at once.

In this paper, we describe the test results for prototypes of the photon-detection, readout, data-acquisition, and primary data-processing systems. All (both hardware and software) principal modules were

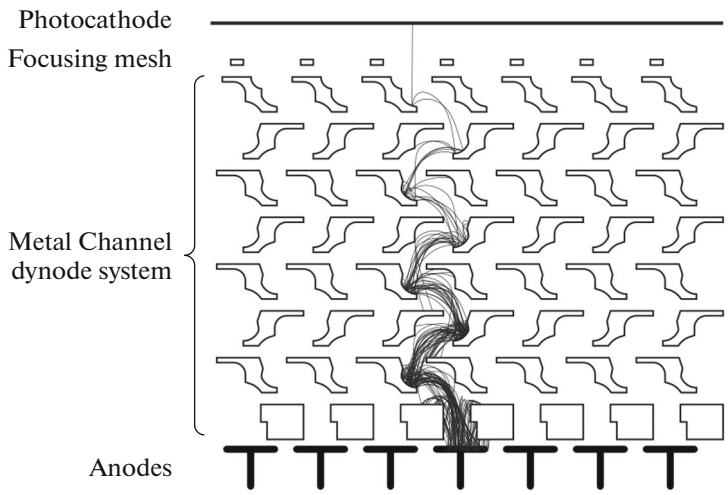

Fig. 2. The diagram of the Metal Channel dynode system.

implemented in the corresponding systems of the Cherenkov-ring detector that is being developed for the CBM experiment. The tests were carried out both in the laboratory and on the beam of the Proton Synchrotron (PS) at CERN, as a part the full-featured prototype of the RICH detector.

2. THE FEATURES OF THE H12700 MULTIANODE PMT

The Hamamatsu H12700 Multianode PMT [16], which appeared on the market in 2013, was characterized in detail in [17]. It has the following advantages: a large fraction of the cross-sectional area is occupied by photosensitive pixels; it has a square shape, which allows large areas to be covered without loss (the packing density is 87%); a single-photoelectron signal transit through the dynode system occurs in a short period of time; a small time from event to event; and low crosstalk as well as a low rate of thermal-electron production. It is superior to its predecessor, H8500 MAPMT [18], in most parameters. Some parameters of an H12700B-03 MAPMT used in the photoelectron-counting mode are presented below.

Typical gain	1.5×10^6
Dark counts per channel, s^{-1}	≈ 10
Dark counts for the entire multianode PMT, s^{-1}	<1000
Pulse rise time, ns	0.64
Spread in the time of electron avalanche development, ns	0.28
Number of Metal Channel dynodes	10

The spectral sensitivity of an H12700B-03 MAPMT used in this work is determined by a bialkali photocathode and an entrance window made of glass transparent to UV light. The short-wavelength limit of the sensitivity spectrum is $\lambda_{min} = 185$ nm, and the quantum efficiency maximum is 33% and is attained at a wavelength $\lambda = 380$ nm. Such spectral characteristics provide detection of Cherenkov radiation in the UV spectral region. An MAPMT channel consisting of a fragment of the dynode system and a photocathode region called a pixel corresponds to each anode. The rms deviation of the gain in the MAPMT channels from the mean value does not exceed 16% [16]. The spread in the quantum efficiency between pixels is, according to our data, $\pm 10\%$.

It has been shown that the radiation hardness of the device is sufficient for use in the CBM experiment [19, 20]. The serviceability of the device in a magnetic field as high as 2.5 mT without a significant drop in its performance was also demonstrated [17]. The use of magnetic shields and the selection of the optimal photodetector location in space make this MAPMT suitable for the CBM experiment.

Along with the listed advantages, the H12700B-03 MAPMT has some features that have no analogs in the traditional MAPMT and require special attention in the development of the readout channel. The multiplication of electrons in the dynode system occurs in the vacuum volume that is common for all channels. Being placed in a single vacuum volume, the dynode system of the Metal Channel type (Fig. 2) [21] is rather compact, uniform for all channels, and capable of providing excellent timing properties.

Electron avalanches that correspond to different channels differ in the location of their passage through the dynode system. Effects are observed, such as the knockout of electrons from dynodes by photons after their passing through the photocathode and the deflection of electrons from an ideal trajectory due to the spread of energies. The latter feature causes electrons to reach subsequent stages of the dynode system, bypassing the previous ones. This results in the flow of the entire electron avalanche or its part to the adjacent

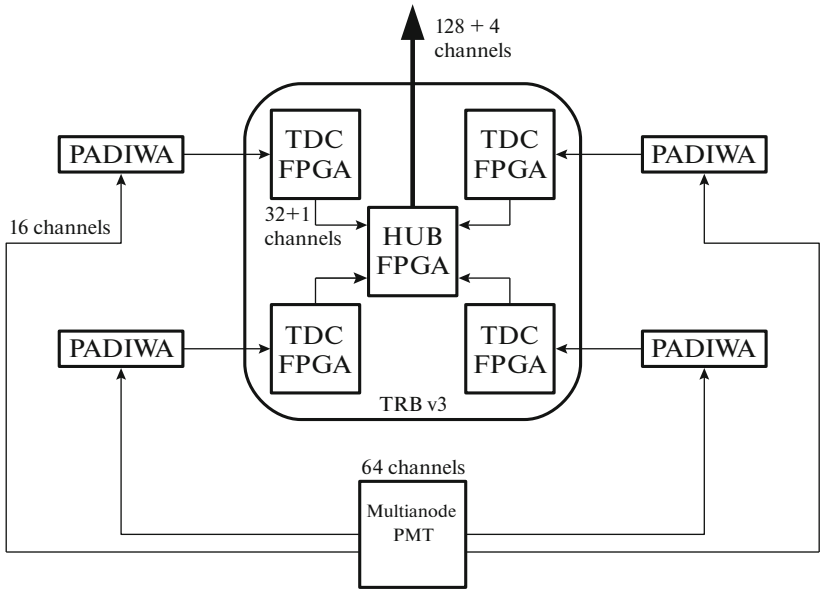

Fig. 3. The block diagram of MAPMT readout consisting of four PADIWA discriminator boards and one TRB v3 board.

channel. The flow of a fraction of the avalanche to an adjacent channel takes place in more than 25% of all cases with the uniform illumination of the entire photocathode. The value of the flowing charge is 3–7%, depending on the relative location of the MAPMT channels [17]. The probability that an avalanche from a photoelectron will fully develop in the adjacent channel depends on the mutual arrangement of the channels and under uniform illumination ranges from 0.1 to 2%.

In addition, in the presence of a relatively large signal in one of the channels, bipolar interference is observed in channels that have their dynodes in a single row. After integration of this interference, low-amplitude pulses may be produced in several channels [22]. In an ordinary single-channel MAPMT, such an effect is not observed due to the absence of coupling with adjacent channels, the presence of an extended focusing system, and a dynode-system design in which the dynodes have a large area and subsequent stages are completely screened by the previous ones.

Owing to the described features, a single-electron spectrum has a low-amplitude part, which merges with the noise and is separated from the main peak by a deep valley. The observation of this effect in our measurements is discussed in Subsection 6.6.

3. THE STRUCTURE OF THE DATA-ACQUISITION SYSTEM FOR THE RICH DETECTOR OF THE CBM EXPERIMENT

3.1. A 64-Channel Readout Module

Physically and functionally, all the electronics for reading and digitizing data from the RICH detector of the CBM experiment can be grouped into 64-channel modules, each of which corresponds to one MAPMT. The block diagram of the 64-channel module is shown in Fig. 3. The module includes four PADIWA boards and one TRB v3 board.

PADIWA is a 16-channel front-end electronic board developed by the GSI [23]. The board is attached to an MAPMT through an adapter card, the only destination of which is to connect the MAPMT anodes with the corresponding inputs of the PADIWA board. On one side of the PADIWA circuit board are 16 signal inputs with an impedance of 100 kΩ. Each input has two contacts: ground and signal.

The board has a connector that allows connection of 20 Low-Voltage Differential Signaling (LVDS) lines. Four LVDS lines are used to control the board, and the other 16 LVDS lines are outputs. A standard JTAG port is provided on the board for programming a field-programmable gate array (FPGA). Each PADIWA channel has its own lowpass filter with a bandwidth of approximately 100 MHz and an NXPBGA 2803 preamplifier, which constitute the analog part of the channel. After amplification, the signal arrives at the FPGA.

An FPGA in each input line has a comparator, via which one can set their own threshold for separating the logical levels of the input signal. Therefore, the adjustable FPGA inputs can be used as discriminators for the analog signal.

The multifunction TRB v3 board contains five FPGAs, each of which can be independently programmed. One central FPGA and four peripherals are used. In our case, four peripheral FPGAs are programmed as a time-to-digital converter (TDC) array, and the central FPGA acts as a data concentrator.

Such a configuration of the board will be called TRB v3 (configuration 1).

The output logical LVDS signals from all 16 channels of the PADIWA board are fed to one of the peripheral FPGAs of the TRB v3 board, where each input channel is split into two TDCs: the first is sensitive to the leading edge, while the second is sensitive to the falling edge of the logic signal at the input. In addition, one more TDC is used to assign timestamps to synchronization signals. Thus, the output of the entire TRB v3 board collects data from 132 TDC. The TRB v3 board has Ethernet ports: both an RG45 and an optical SFP, which are used for two-way communication with other TRB v3 boards or with a computer.

All peripheral FPGAs are divided into a number of areas, in each of which the same TDC circuit is programmed. These circuits are located in different areas of the array; thus, each TDC has its own signal path length traveled inside the FPGA.

A pulse from one input channel is processed by two TDCs, the relative delay between which must be calibrated using a precise rectangular-pulse generator. Note that for each TDC an FPGA has an individual counter of recorded timestamps, whose value can be interrogated regardless of the main data stream. Such a counter can be used, e.g., to obtain the dependence of the counting rate on the discriminator threshold in order to determine the optimum threshold.

A time measurement in the TDC is carried out in two stages. The clock generator with a period of 5 ns controls the ring counter. The 28 high-order bits of this counter are called the epoch, while the 11 low-order digits are called the coarse time [24]. When measuring the time of the leading edge input signal, the time value is encoded by two messages: the epoch and the timestamp. To reduce the output stream, the value of the epoch, which increases every 10/24 μs, is transmitted once for a group of timestamps belonging to this epoch.

An additional 10-bit register is used for measurements with a higher accuracy. The value of the fine time obtained from the digital delay line with taps on 512 effective elements is written to the register. Because of the imperfection of the components, scatter occurs in the parameters of the elements in the delay line; therefore, the results of fine time measurements must be calibrated with respect to the range of register values. The calibration procedure is discussed in Subsection 5.2.

The FPGAs on the TRB v3 board form 4-byte messages of one of the following types: EVENT, SUBEVENT, SUBSUBEVENT HEADER, TDC HEADER, EPOCH COUNTER, TIMESTAMP, and DEBUG. The logic for generating messages is described in detail in the documentation [25].

It should be noted that each readout channel is characterized by some individual delay between the moment of photoelectron production and the timestamp of the leading edge. This delay is determined by the time of the electron-avalanche development in the dynode system, the propagation time of the signal along the conductors, and the switching time of the logic elements. The procedure for correcting delays and its features are described below, in Subsections 5.3 and 6.2.

3.2. Data Concentration and Inputting to a PC

The concept of the data-acquisition system for the CBM experiment includes four functional levels, each of which is implemented by corresponding boards. In the general case, the front-end board (FEB) that is used to perform analog conversions and signal digitization is adjacent to the detector. Further, the data in the form of electrical digital signals are fed to the readout board (ROB), where the data are concentrated and transferred via an optical channel. At the next level, there are data-processing boards (DPBs). The DPBs compress data from various detectors by removing redundant information in a way specific to each detector and group these data into packets called the time slices.

Each time slice contains messages from a certain group of readout channels with a timestamp in a predetermined interval. Further, they are transmitted over optical channels that are fewer in number and feature a higher throughput [26]. The data are then transferred to the memory accessible to the central processor of a computer over a high-speed bus through the interface boards, called the FLIBs. The abbreviation FLIB denotes the FLES interface board, and, in turn, the FLES [27] is the first-level event selector, i.e., a specialized hardware and software system for constructing events "on the fly" and selecting them according to specified criteria. The FLIB can be implemented, e.g., by programming a commercial PCI-E HTG K-7 card.

In the case of beam tests, the RICH front-end electronic board is a pair of PADIWA–TRB v3 (configuration 1). In the future, it is planned that the functionality of these boards will be combined on a single DIRICH board [28]. A TRB v3 card configured as a concentrator is used as a ROB. The DPB is at the prototype development stage, while the FLIB has been used for the first time in one of the tested versions of the data-acquisition system. A significant part of the measurements were performed using a stable data-acquisition system based on the data-acquisition backbone core (DABC) [29] and a conventional network card.

4. EXPERIMENTAL SETUPS

4.1. The Experimental Setup for Beam Tests

The system of reading and data acquisition was studied as part of a full-featured prototype of the RICH detector for the CBM experiment during comprehensive beam tests of several prototype detectors

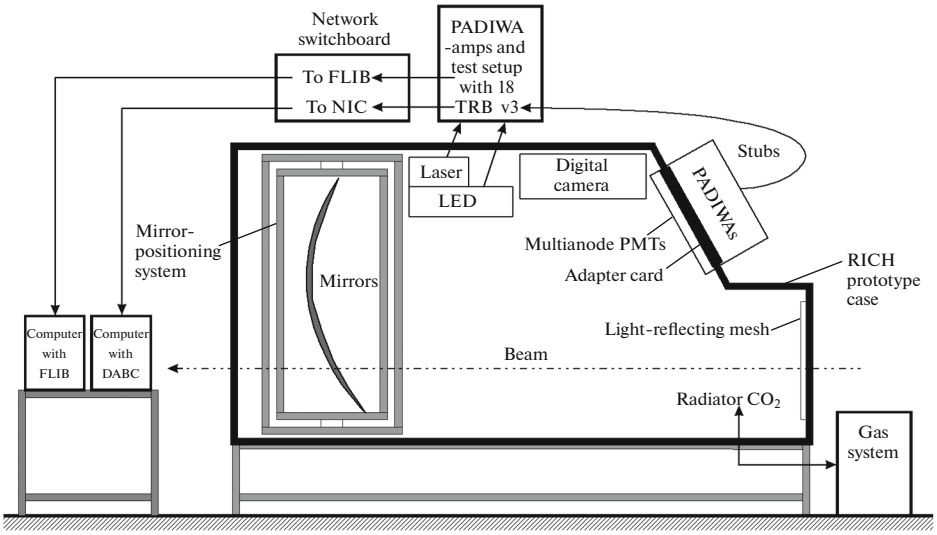

Fig. 4. The diagram of the RICH detector prototype.

for the same experiment [30]. The design details of the transition-radiation and TOF prototype detectors were presented in [31] and [32], respectively.

The tests were conducted on the T9 beamline of the PS at CERN [33]. A mixed secondary beam consisting of electrons, pions, and muons with a momentum adjustable in the range of 0.5–10 GeV/c was used. During the tests, the beam was tuned to momenta of 1–3 GeV/c. The spill duration was approximately 2 s and 500 electrons were detected for this time, on average.

The diagram of the RICH detector prototype for the CBM experiment is shown in Fig. 4.

The aluminum case of the RICH detector is hermetically sealed and is 1.4 m wide, 1.2 m high, and 2.4 m long downstream of the beam, while the path length of a particle in the radiator to the mirrors is 1.7 m. The detector radiator is carbon dioxide at an excess pressure of 2 mbar at room temperature. The refractive index of the gas for the near UV spectrum range is $n = 1.00045$. The cleaning of the gas and the stabilization of its pressure with an accuracy of 0.1 mbar were provided by the gas system described in [34]. The absolute pressure of the gas mixture and the temperature are monitored by a slow control system. The current refractive index value is automatically calculated and stored with data.

The mirror-positioning system was described in detail in [35]. A mirror-position diagnostic system [36] is also used, which consists of a reflective mesh that occupies the entire front wall of the prototype body, a Roithner UVTOP240 LED [37] with a wavelength of 245 nm, and a digital camera that is read remotely. The system allows one to determine the deviations of individual mirror parts and the corrections to the rotations of individual mirror parts and calculate corrections to the coordinates of hits (detected photons).

Cherenkov radiation is focused by mirrors on a photosensitive chamber that contains an array of 4 × 4 MAPMTs, six of which are Hamamatsu H12700 and ten are Hamamatsu H8500 tubes. These MAPMT models have a cross section of 52 × 52 mm^2. Some MAPMTs were preliminarily covered with a layer of a wavelength shifter (WLS) 150–200 nm in thickness. Paraterphenyl (≈40 wt %) in a Paraloid B72 (polymethyl acrylate) polymer matrix was used as a WLS.

The WLS was applied by immersion in a solution of coating components in dichloromethane; see [38]. The WLS was scraped off at a certain time during the beam test. This made it possible thereafter to estimate the influence of the WLS on the single-photon detection efficiency and on the time variation of hits that belong to the same ring.

An Alphalas Picopower LD405 laser [39] was used along with an LED to monitor the readout system and calibrate the inter-channel delay. This laser emits at a wavelength of 405 nm; its nameplate pulse width is less than 40 ps. The operating frequency of the laser, as well as of the LED, was 100 Hz. The laser intensity was selected so that the response frequency of each pixel was approximately 10% of the operating frequency of the laser.

Data were read out of each MAPMT by the module described in Subsection 3.1. Mechanically, all the 16 MAPMTs were mounted on the adapter card, which ensured the tightness of the case and wiring of the high voltage. The PADIWA preamplifier–discriminator boards were mounted on the adapter card from the outside. The logical signal from these boards was transmitted to the TRB v3 (configuration 1) boards attached to the prototype case over stubs consisting of 2-m-long

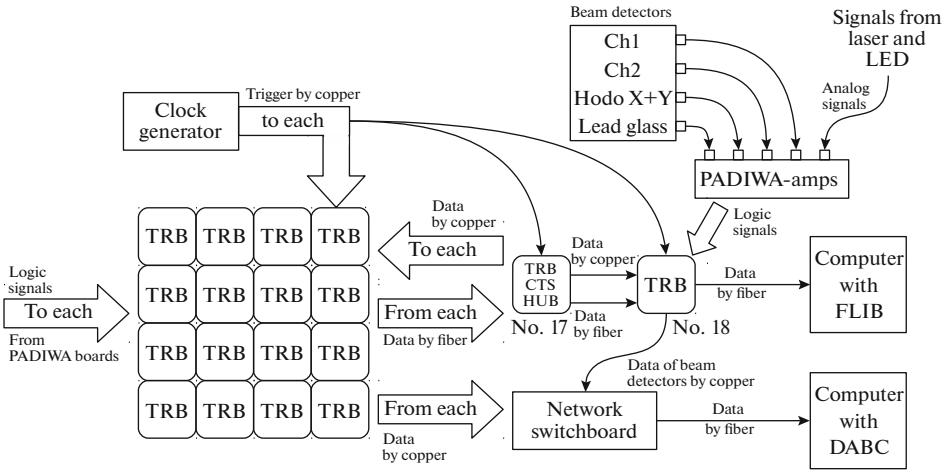

Fig. 5. The layout of readout of the entire chamber and the beam detectors: (*TRB*) TRB v3 with standard firmware of four TDCs and "a hub," four expansion cards are the adapters for stubs that receive logical LVDS signals from the PADIWA boards; (*TRB CTS HUB*) TRB v3 with the "CTS + 4hubs" firmware; and (*CTS*) Central Trigger System, four expansion cards, each with eight input optical ports, the trigger from one RG45 output is distributed through the special "LVDS fanout" boards.

twisted pairs. A total of 64 PADIWA boards and 16 TRB v3 (configuration 1) boards were installed in the entire chamber. The data from the 16 TRB v3 boards were fed to the additional (17th) special-configuration TRB v3 card, which was, apart from the data concentrator, also a generator and a distributor of the readout trigger for all TRB v3 boards.

Pulses from generators that control the laser and the LED, as well as signals from the beam detectors, were processed by PADIWA-amp boards (a board that is similar to PADIWA, but allows signal-amplitude measurements and has half the number of channels [23]) and digitized by a TDC on one more, the 18th, TRB v3 card. This card also has a non-standard configuration and combines the functions of the TDC and the data concentrator. Two data-acquisition systems functioned in parallel: one received data via a standard network interface (a network hub) from each TRB v3 card via a copper carrier and the other received data via the FLIB from the 18th TRB v3 card. The layout of reading the entire chamber and the beam detectors is shown in Fig. 5. We note that a computer with the FLIB installed in it was used to receive data not only from the prototype of the RICH detector, but also from other detectors.

4.2. The Laboratory Test Setup

The PADIWA board-based readout system was first used in the beam tests of the CBM experiment in November 2014. The simplest analysis of the data obtained showed that some timestamp distributions lacked an obvious explanation. This required assembling a laboratory stand with which it was possible to study the features in the operation of one multichannel module of the readout system described in Subsection 3.1 in more detail. In some measurements, the output LVDS signal from the PADIWA board was not digitized by the TDC, but was read out by an oscilloscope using an active probe.

For a better understanding of the operation of the readout and data-acquisition system, a more informative but slow version of the system for readout and data acquisition based on a 128-channel n-XYTER chip was created at the same laboratory test setup. Each channel of this chip measured the arrival time of the leading edge and the amplitude of the input signal. The system consists of a front-end electronics board that is connected to the MAPMT via a printed-circuit-board–adapter and to the computer via the SysCoreROC readout controller [40]. For readout of one MAPMT, it is enough to use 64 channels, i.e., half of the channels of one front-end electronics board.

The diagram of the laboratory test setup is shown in Fig. 6.

The test setup is enclosed in a light-proof body measuring 80 × 80 cm and 2 m long. The laser used in the beam tests was also used here as a light source. The laser light was delivered into the case over a fiber. In order to provide uniform illumination of the MAPMT surface, the laser light passed through a scattering frosted glass.

The laser intensity is matched so that the channels of the MAPMT work in the single-electron mode. The average frequency of recording photoelectrons in each channel is approximately 10% of the frequency of the laser pulses.

The H12700 MAPMT was located at a distance of ~30 cm from the scattering glass. The scattering glass and the MAPMT were enclosed in a black plastic pipe, which in turn was placed in a light-proof housing. To reduce the dark counts, the MAPMT was kept in the dark for at least 1 h before starting measurements.

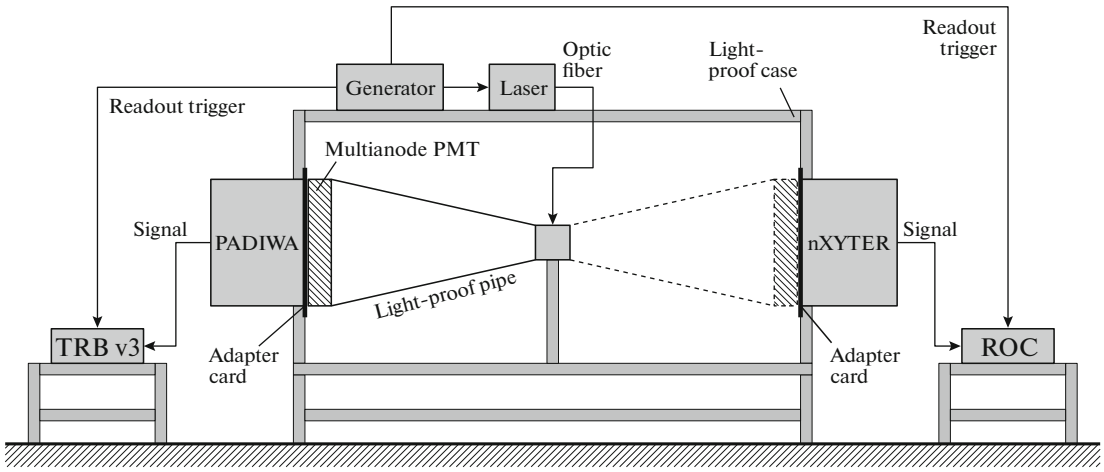

Fig. 6. The layout of laboratory setup: (ROC) readout controller.

Two systems of readout and data acquisition were installed simultaneously, each on its side of the case. The above-mentioned plastic pipe, the scattering glass, and the MAPMT rotate as a unit, providing the same illumination conditions for of the MAPMT in positions that correspond to the operation with both readout systems.

Both systems of readout and data acquisition are self-triggered in the sense that each pulse at the input, upon overcoming the preset threshold, is measured and entered into the output buffer. However, for the data from the output buffer to be sent to the computer, a read pulse must be periodically sent to the auxiliary input of the readout controller. In our setup, the pulses of the laser-controlling generator act simultaneously as a trigger for reading the output buffer.

In the used systems of readout and data acquisition, the read trigger automatically enters the input data stream. This makes it possible to analyze the recorded time stamps, comparing them with the moment of the laser pulse. The data were sent from both systems of readout and data acquisition via a standard Ethernet cable to the network interface of the computer.

5. THE SOFTWARE

The software for the system of readout and data acquisition of the RICH detector prototype for the CBM experiment is a set of modules for data reception, primary processing, and storage, which are all implemented within the CbmRoot software framework [41]. CbmRoot, together with FLESnet [42], forms an infrastructure that allows reception, simulation, reconstruction, and analysis of data in the CBM experiment.

All stages, from data readout to analysis, can be performed "on the fly," without recording intermediate results on the disk. In the course of the tests described in this article, the data-processing sequence shown in Fig. 7 was used. The software implementation, functionality, and interaction of individual units are described below.

5.1. Unpacking

Unpacking is the first stage in the processing of data that come from the electronics. In CbmRoot, it is possible to process both data that arrive directly from detectors and that are being saved to a file (using the DABC in the HLD–HADES list mode data format [43]). When using the FLIB, unpacking is preceded by the launch of a small interface module that extracts messages related to the RICH detector from the FLESnet data stream in the time slice archive (TSA) format. Unpacking is implemented as a CbmRichTrbUnpack task class. As a result of execution of each iteration, TClonesArray with objects of the CbmTrbRawMessage class is formed at the output.

5.2. The Fine Time Calibration

The procedure for calibrating fine time embodies the well-known technique for calibrating a digital delay line with taps [44]. The calibration technique is based on the fact that the distribution of the signal-arrival times must be uniform over the time interval occupied by all delay elements. Upon analyzing a portion of the acquired data for each channel, a discrete $f_{\text{calib}}(\text{Fine})$ function is constructed, i.e., a table for transition from the register value to the fine time in nanoseconds. When using the fine time calibration table, the total time is calculated as $T\,[\text{ns}] = \text{Epoch} \times 2048 \times 5 + \text{Coarse} \times 5 - f_{\text{calib}}(\text{Fine})$.

The fine-time calibration procedure is implemented in the CbmTrbCalibrator singleton class, which is not a part of the data-processing pipeline; i.e., access to an object of this class can be performed from any place in the program. The possibility exists to

save calibration tables to a separate file, which speeds up multiple calculations due to repeated use of once-calculated tables. The features of the fine-time calibration functions and their effect on the time resolution were discussed in detail in our works [45, 46].

5.3. Inter-channel Delay Correction

To correct inter-channel delays, the CbmTrb Calibrator class makes it possible to import a correction table built in advance using the CmbRoot macros Extract Delays and Build Delta Table based on the results of the first data analysis run.

The algorithm for correcting delays is as follows. Let use introduce continuous numbering of pixels over the entire photosensitive chamber consisting of many MAPMTs. The total number of pixels is $M = 64N$, where N is the number of MAPMTs. All leading edges with a timestamp that falls within a preset time window with reference to the laser triggering are selected for the analysis. The window is selected in accordance with the distribution constructed for a specific data set. Usually, the width is approximately 100 ns and the left boundary is shifted for 20 ns from the moment of laser triggering. Throughout the array of selected data, histograms of the difference between the timestamps of the ith and jth channels are constructed, where i and j run through values from 1 to M. As a measure of the inter-channel delay difference, the user can take, at their choice, either the average or the most probable value of the distribution. The obtained values are used to fill a skew-symmetric matrix A with dimensions of $M \times M$. Afterward, the user can define the reference channel relative to which the correction table will be created, which is actually a column of the matrix A.

5.4. Reconstruction of a Hit

The set of information about each detected photon, called a hit, consists of two messages containing timestamps of a front and a trail of a logic signal. Since different channels have different delays and the probability of measuring individual logic swings is not 100%, it is necessary to implement a algorithm for matching front–trail pairs in the data analysis. This procedure has been implemented in the CbmTrb Edge Matcher task class that is located in the pipeline after the unpacking and is actually executed after applying all calibrations.

A message buffer was created for each input channel, This buffer was filled with objects containing information about fronts as they arrived. Further, as soon as a trail came, a front with the closest timestamp was selected from the buffer within a preset permissible time window. The time over threshold (ToT) is the parameter of a hit that indicates the signal amplitude. It is calculated as the difference of the timestamps of the trail and the front in the matched pair.

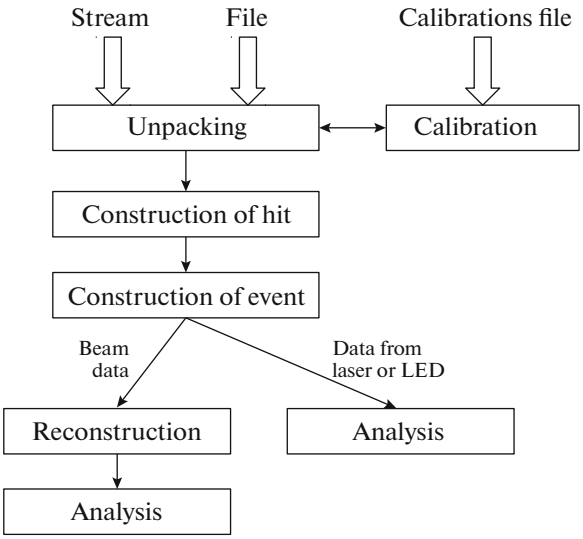

Fig. 7. The diagram of interaction of the software modules.

Since the corresponding paired front or trail is sometimes absent, the buffer is filled gradually, and it must be cleared to avoid overflow. If there is no candidate front in the buffer for the arriving trail, this means that the front has not been recorded. In this case, this trail is discarded. The number of fronts and trails that are not found depends strongly on the loading of the input channel, which in turn depends on the discriminator threshold. At a low threshold, high-frequency electronic noise is recorded, which leads to a huge flow of output messages that cannot be transmitted due to the limited capacity of the output section in the readout system.

It is possible to accept single fronts as hits, but practice has shown that this makes no sense, since in normal mode, the unidentified pairs are mainly due to TDC errors, and the proportion of such messages is negligible, less than 2×10^{-4}.

5.5. Event Construction

Data are received in portions called “the DAQ events,” which are in no way associated with real events. To generate correct input information for reconstruction and further analysis of data, it is necessary to perform a procedure for constructing an event, which was described in detail in [45].

5.6. Reconstruction

In the CBM experiment with the RICH detector, reconstruction means the search for rings by hits in the reconstruction plane. In the context of reconstruction, a hit may be considered as an excited MAPMT pixel. After focusing by mirrors, a cone of Cherenkov photons intersects the surface of the photosensitive chamber, which in general may consist of several

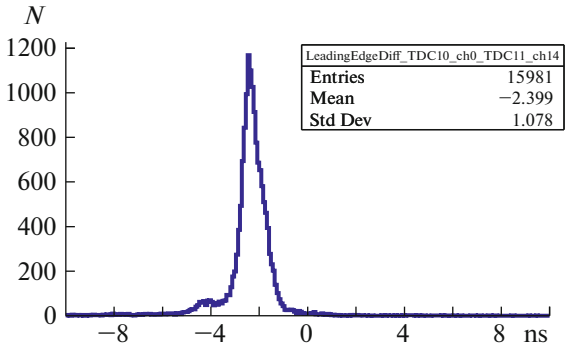

Fig. 8. The distribution of the difference in timestamps of the fronts corresponding to photons from a single laser pulse recorded in a prescribed pair of channels.

planes. The first stage of reconstruction is the translation of hits from the chamber planes to the reconstruction plane. Then, rings are searched for by hits. In CbmRoot, there are several algorithms for finding rings. A matter of the greatest practical interest is the algorithm for recognizing Cherenkov radiation rings based on the Hough transform and described in [47, 48]. The implementation of this algorithm was specially adapted to beam test data in which one ring per event is expected. This algorithm is implemented in the CbmRichProtRingFinderHoughImpl class, inherited from CbmRichProtRingFinderHough and, further, from CbmRichRingFinder. After this, the parameters of the ring are determined and particle tracks are reconstructed using information from other detectors.

6. RESULTS

6.1. Testing of the Data-Acquisition System Using the FLIB

A significant part of the data was collected in parallel by the two data-acquisition systems. The byte-by-byte comparison of the unpacking results from both streams was performed. No discrepancies were revealed in an array of approximately 10^7. Therefore, the efficiency of the concept for forming time intervals and inputting data into a computer using the FLIB has been demonstrated. The results in the following sections are based on data received through a standard network interface using the software based on the DABC [29].

6.2. Determination of the Inter-channel Delay Corrections

A typical histogram of the difference in the timestamps of the fronts corresponding to photons from a single laser pulse, which were detected in a prescribed pair of channels, is shown in Fig. 8. Such histograms help to determine the position of the peak and, hence, introduce a delay correction. Note that an uncorrelated drift of approximately 0.5 ns in observed for individual values of the delays obtained in such a way that it makes a significant contribution to the time resolution of the readout system (see Subsection 6.3).

The additivity of delays is also observed; i.e., the delay in the *i*th channel relative to the reference channel can be obtained with an accuracy of at least 400 ps as the sum of the delay in the *j*th channel relative to the reference channel and the delay in the *i*th channel relative to the *j*th channel. For some channel pairs, the histogram is different from the one shown in Fig. 8; e.g., see Fig. 9. A similar distribution can be obtained if one of the two channels is defective in the sense that an excited or induced oscillation signal is mixed to the front of the logic signal. This hypothesis is confirmed by the fact that the histogram shape depends on the discriminator threshold on the PADIWA board. When constructing a similar histogram for a pair of defective channels, as many as five peaks are observed in the histogram. Further investigation was conducted with the exclusion of defective channels. The share of defective channels is approximately 10% of the total number of channels. In developing the next version of the front-end electronics for the RICH detector of the CBM experiment, special attention will be paid to the electromagnetic cleanliness of the channels and histograms similar to those discussed in this section will be used as a diagnostic tool.

6.3. The Time Resolution

In the performed beam tests, there are two types of events in which several simultaneously emitted photons are detected. The first type is a laser pulse, whose duration is ~40 ps, i.e., smaller by an order of magnitude than the spread in the signal transit time through the MAPMT. The second type is a Cherenkov ring. The spread of the arrival time of photons at an MAPMT may reach 100 ps for rings and 70 ps for laser pulses, which is determined primarily by the slope of the plane in which the photocathodes are located. Analysis of such events allows us to characterize the time resolution of the entire readout system, starting with the entrance window of the MAPMT and ending with the production of timestamps.

The time resolution of one channel is determined by the spread of the recorded timestamps relative to the photon-arrival time in repeated measurements. Since the fine time of photon arrival cannot be measured, we must investigate the spread in the differences of timestamps in a pair of channels when detecting simultaneously arriving photons.

The timestamps in each channel are subject to independent fluctuations according to the same law; therefore, the measured distribution width will be $\sqrt{2}$ times greater than the time resolution of each channel. After applying delay corrections and calibrating the fine time in two channels, none of which is defective,

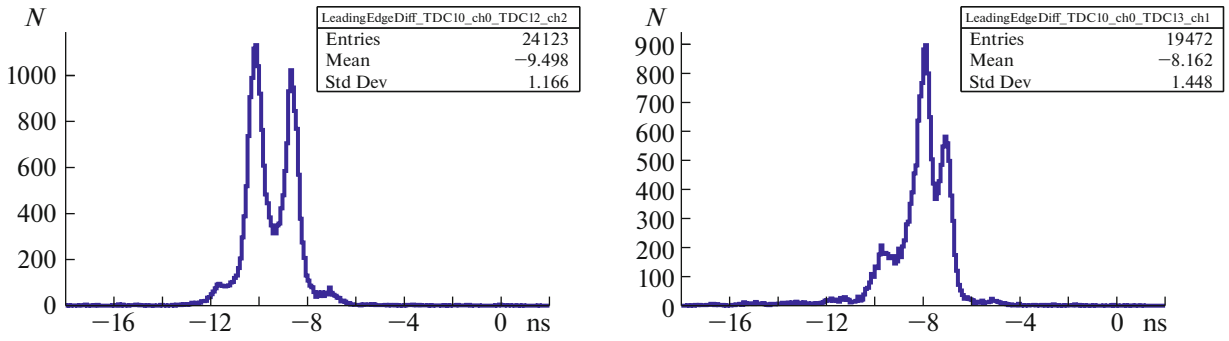

Fig. 9. The distributions similar to those shown in Fig. 8 provided that one of the channels is defective.

a distribution similar to the distribution shown in Fig. 8 is obtained; it differs only in that the peak center is at zero.

The full width at the half-maximum (FWHM) of this distribution is 750 ps, which corresponds to a time resolution of 530 ps. This value exceeds the spread of signal transit times in an MAPMT by approximately two times. The discrepancy can be explained by two comparable contributions: the drift of the delays in the channels and the absence of a correction of the threshold-crossing time depending on the signal amplitude. To perform such a correction, a reliable measurement of the time over the threshold is required, which in our case is impossible (see Subsection 6.5).

In order to characterize the time resolution of the entire system, in addition to analyzing channel pairs, physically simultaneous signals were studied on the following sets of channels: (i) up to 16 channels read by a single PADIWA board; (ii) up to 64 channels belonging to one MAPMT; and (iii) up to 256 channels belonging to four adjacent MAPMTs. In each case, after correcting the delays and calibrating the fine time, all hits belonging to one event were selected and histograms of the timestamp difference were constructed for all possible channel pairs (Fig. 10).

Since a Cherenkov ring focused at a region of four adjacent MAPMTs is projected onto only a fraction of the pixels, the actual number of investigated channels is different in the case of Cherenkov rings. The table shows how the rms deviation and FWHM evolves depending on the number of channels. Note that the rms deviation varies only slightly, and the FWHM increases with the number of channels. At the same time, the distribution takes a form that is closer to the Gaussian distribution.

Similar distributions were also constructed for the case when the WLS was applied to the MAPMTs. The results are also displayed in Fig. 10 and in Table 1. In some cases, the maxima are shifted from zero within 100 ps, which is due to the difference in the light path to different pixels.

6.4. Investigation of the WLS Emission Profile

An analysis of the time distribution of hits belonging to a single Cherenkov ring makes it possible to

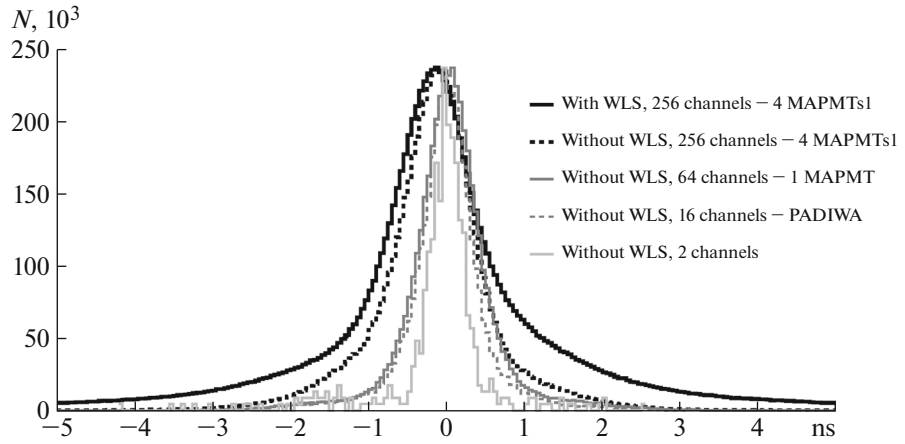

Fig. 10. The distributions similar to those shown in Fig. 8, corresponding to photons from one Cherenkov ring for four sets of channels.

Table 1. The FWHM and RMS for the distributions of timestamp differences for different sets of studied channels

Analyzed region	Pair of channels	PADIWA board	One MAPMT	Four MAPMTs
Number of channels	2	14	39	131
FWHM (rings, without the WLS), ns	0.40	0.60	0.80	1.05
RMS (rings, without the WLS), ns	0.66	0.58	0.62	0.79
FWHM (rings, with the WLS), ns	0.55	0.75	0.95	1.25
RMS (rings, with the WLS), ns	1.48	1.35	1.35	1.47
FWHM (laser), ns	0.7	1.05	1.30	1.55
RMS (laser), ns	0.83	0.79	0.85	1.04

Note: WLS is the wavelength shifter.

study the timing properties of the WLS. We must analyze the distribution of the differences of hit timestamps in each ring with respect to the hit that was the first in time in a certain ring. Depending on the wavelength, a Cherenkov photon, with some degree of probability, can either be absorbed by the WLS and cause its luminescence or pass through the WLS layer without interaction and hit the photocathode.

As a result, even in the presence of a WLS layer, some of the hits obey the time dependence that is characteristic of a pure PMT. Thus, in order to obtain the WLS luminescence curve, it is necessary that the time-differences distribution obtained with the pure PMT and properly normalized at the maximum be subtracted from the time-differences distribution of obtained with the WLS.

The luminescence curves with and without the WLS, after being normalized at the maximum, are shown in Fig. 11; the difference of these distributions is shown in Fig. 12. It can be seen that the curve looks like the sum of several exponentials, with the exception of a small convexity in the region of 7 ns, which is associated with the peculiarities of operation of this MAPMT family.

This convexity makes it impossible to reliably determine the characteristic luminescence times. It is interesting, however, to compare the obtained curve with the results of fluorometric studies. A glass plate with a WLS layer applied in exactly the same way as on the MAPMTs was investigated using the classical method of photon counting upon excitation by light with a wavelength of 280 nm. The decay times were 1.4, 3.8, and 45 ns, and the corresponding relative intensities of the components were 1.8996, 1.0000, and 0.8364.

Fitting the curve in Fig. 12 by the sum of three exponentials with the respective times shows reasonable agreement for times exceeding 5 ns. The initial segment is fitted better at $\tau_1 = 1.1$ ns. Comparison of the intensities of the fastest component with the fluorometric measurements is difficult due to the initial non-exponential segment and the relative contribution of the slowest component to the total intensity in our case is lower by a factor of 3.8. This can be explained by the influence of the excitation method on the population of the centers of excitation of different types.

In the limit of a large number of hits in a ring, the method we used goes over into the standard method for studying fluorescence by counting single photons [49]. However, in our case, there is a random delay between the moment when a Cherenkov photon hits the MAPMT surface and the arrival time of the first hit. A Monte Carlo simulation was performed to determine the effect of the method on measured decay times.

The model included a 300-ps (rms) spread of the avalanche transit times in the MAPMT, three exponential components with characteristic times of 1.4, 3.8, and 45 ns and relative intensities of 2.17, 1.00, and 0.22, and the average number of hits in the ring equal to 18. The resulting time distribution relative to the first hit in the ring was fitted by three exponents with free parameters. If we start fitting the resulting dependence after 4 ns from the start of the luminescence, the decay constants of the exponents are reproduced with an accuracy better than 5%, while the corresponding relative intensities are somewhat distorted, which is natural due to the existence of the initial non-exponential segment of the curve. Thus, the correctness of the method used to determine the decay times has been verified.

The practical value of our study lies in the feasibility of optimizing the duration of the window within which hits are accepted as simultaneous and can be

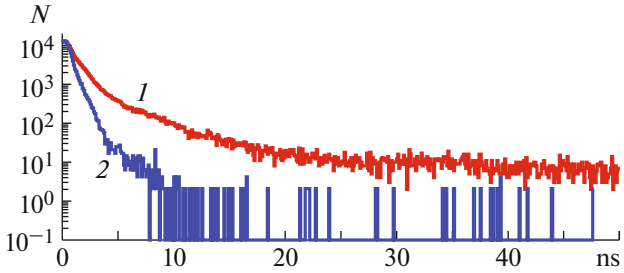

Fig. 11. The measured distributions that correspond to the decay curves (*1*) with and (*2*) without the WLS.

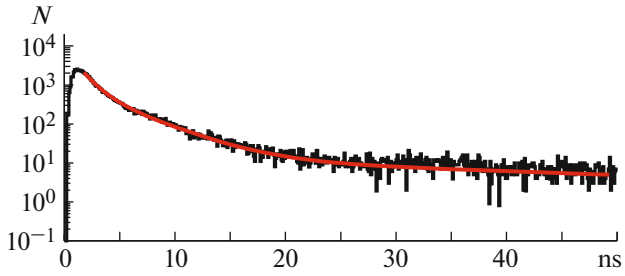

Fig. 12. The difference of the distributions with the WLS and without it; the curve is the fit of the distribution by the sum of three exponentials.

attributed to one event. To do this, it is necessary to find a balance between the number of additional hits obtained due to the WLS and the probability of signals overlapping or picking a dark hit up into the ring. As an example, a 19% increase in hits can be achieved with a window length of 15 ns.

6.5. The Time over a Threshold

The time over threshold (ToT) is a parameter of a found hit, which contains information about the amplitude of the recorded signal during normal operation. In the readout and data-acquisition system of the RICH detector for the CBM experiment, the ToT parameter can be used to improve the time resolution by correcting the threshold-crossing time in view of the walk correction, as well as to improve the quality of separation of the single-photoelectron signal from noise.

Figure 13 shows the typical ToT distribution measured with a laser in the laboratory. Contrary to expectations, this distribution has several peaks. Such a structure, according to [50], can be explained by the presence of periodic noise pickup both at the input of the discriminator, and between the discriminator output and the TDC input. Figure 14 shows the digital oscilloscope screen in the mode of acquisition of signals obtained by connecting the active probe to the PADIWA output.

It can be seen that (i) the signal thickening corresponds to the observed peaks in the ToT distribution; (ii) the problem occurs that the amplitude of a single-electron signal is insufficient for stable generation of logical unity; (iii) periodic noise pickup occurs at the output of the discriminator, but it is not enough to explain the observed picture; and (iv) the predominance of certain durations of logical signals allows us to assume the presence of a periodic structure in the input signal.

All these facts reveal the need to adjust the analog part to form a cleaner signal with a larger amplitude at the PADIWA input and to protect the connection between the discriminator and the TDC from the interference. Such changes will be made, taking the

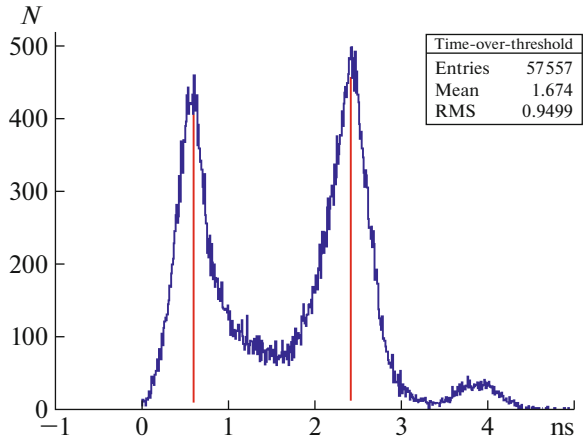

Fig. 13. The typical ToT distribution.

results of this work into account, in the next prototype of the front-end electronics board, which will be called DIRICH [28].

Note that, in the case of the RICH detector for the CBM experiment, these problems are not critical and the parameters shown in this paper are sufficient for a confident search for rings. Nevertheless, improving the separation of signals and noise and increasing the detection efficiency will help to create the necessary margin of safety for long-term operation of the detector under gradual degradation of the optical properties of the radiator, mirrors, and photodetectors.

6.6. Comparison of Single-Electron Spectra for Timing and Amplitude Readout

As noted in Section 2, an H12700 MAPMT has features that can affect the detection efficiency for single photoelectrons and the probability of false hits. To reveal these features, the amplitude distributions were measured using a multichannel board based on the n-XYTER chip (see the description of the laboratory test setup in Subsection 4.2). The results of the amplitude measurements were then compared to the data obtained with the PADIWA board.

The amplitude measurements with a low threshold demonstrated the presence of a discernible peak at small amplitudes in the event spectrum correlated with the light source. The measurements were also made with a mask that opened only two pixels separated by 2.5 cm. These measurements have made it possible to establish that an event with a small amplitude in one of the channels occurs when another photoelectron with a sufficiently large amplitude was detected in another channel in the same row of the dynode system. Thus, for channels with low noise, the amplitude spectrum of single-electron signals has the form shown in Fig. 15.

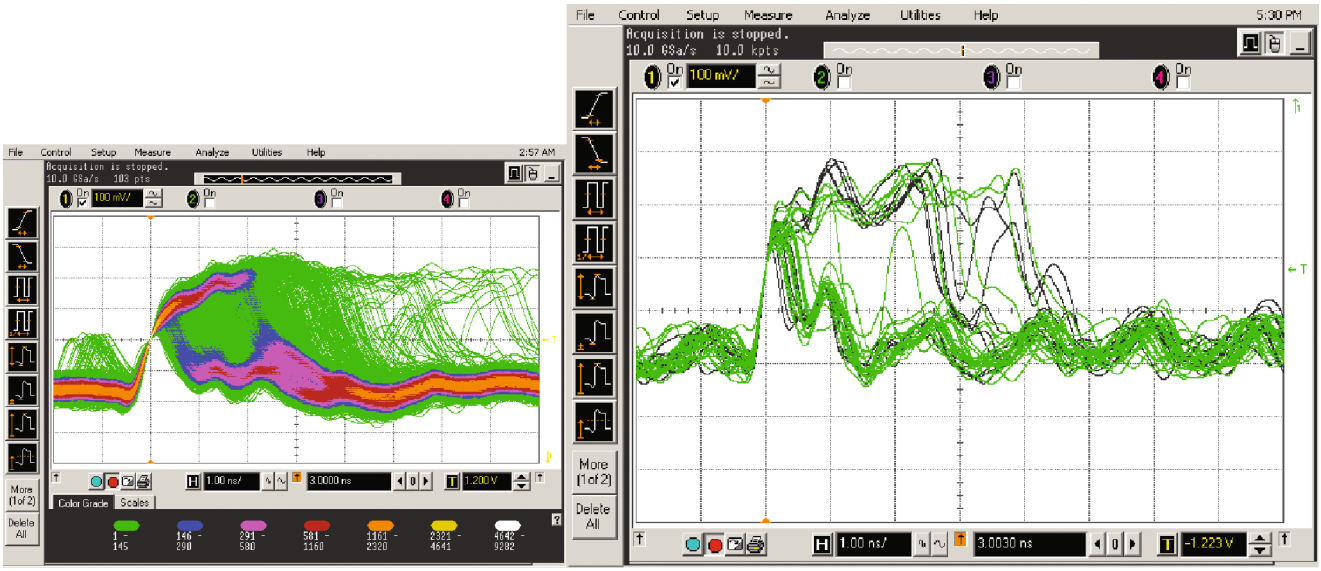

Fig. 14. The oscilloscope screen showing the PADIWA output signals recorded by their front. The right and left panels of the figure differ in the acquisition time.

A peak near zero corresponds to noise pickup occurring in channels of the same row as the channel where the single-electron signal was recorded. The two-peak distribution on the right corresponds to real single-electron signals. In this case, the left peak is related to events described in Section 2, which correspond to the deviation of the electron avalanche or its part from the optimal path from one dynode to the other.

Note that, in most channels, the noise level is too high to separate the low-amplitude peak associated with the noise pickup from the single-electron signal. Thus, an attempt to obtain the maximum detection efficiency by lowering the threshold leads to an increase in the number of parasitic hits localized on pixels other than those where a photoelectron was produced. To reduce the number of parasitic hits, we set the detection threshold in the hollow between the low- and high-amplitude parts of the one-electron spectrum. Since the shapes of single-electron spectra in all channels are similar, analysis of the spectrum shape in Fig. 15 suggests that the selected threshold leads to a loss of 12% of single-electron pulses.

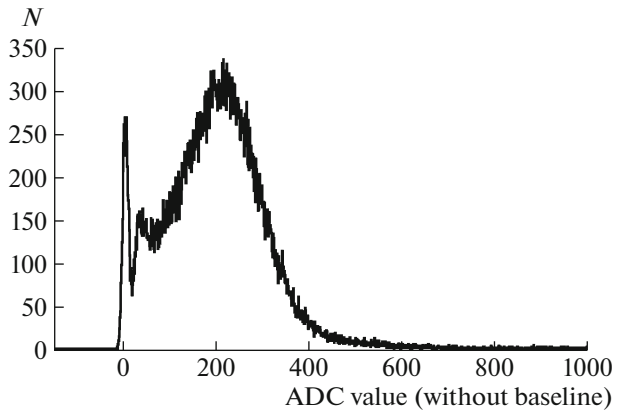

Fig. 15. An example of the measured single-electron spectrum, which has a special shape characteristic of an H12700 MAPMT.

One of the differences of the readout channel in the PADIWA board is that it is much faster than the analog part in n-XYTER. Although the n-XYTER board form signals with an integration time of 190 ns, the PADIWA board performs only the suppression of frequencies higher than 100 MHz, which corresponds to the characteristic pulse rise time of several nanoseconds. This difference leads to an increase in the role of fast noises and pickups when recording signals using PADIWA.

Information on the shape of the single-electron spectrum when read out by a channel on the basis of the PADIWA and TRB v3 boards can be obtained in the form of the counting rate in events occurring near the light pulse as a function of the detection threshold. The use of the counter of recorded fronts, realized directly in the TDC and mentioned in Subsection 3.1, makes it possible to obtain a similar dependence at maximum frequencies sufficient for the baseline localization, but without selection of events around the light pulse.

Figure 16 shows the dependence of the front-recording rate on the detection threshold. The plateau on the left corresponds to the single-electron spectrum, which is examined in more detail below. The rapidly increasing boundaries around the vertical dashed line limit the localization of the baseline. The

accuracy of baseline localization is estimated as ±100 counts on the scale used in Figs. 16, 17b, and 17d.

It has been established that the measured counting rate obtained with the counter and from the analysis of the data stream coincide if the system of data acquisition and transmission copes with the transmission of the message stream with timestamps.

It is interesting to compare the dependence of the counting rate on the threshold when using two readout systems and the same exposure conditions. The results of such a comparison for one of the typical channels are shown in Fig. 17. In the case of the n-XYTER board, the single-electron spectrum integral shown in Fig. 17c can be used for this comparison. Therefore, the derivative of the above dependence obtained with the PADIWA board can be compared with the single-electron spectrum obtained with the help of the n-XYTER board (see Fig. 17a). The solid line in Fig. 17b was obtained by differentiating the curve shown by the solid line in Fig. 17d and obtained by fitting the measured dependence with a polynomial of the seventh degree. We note that according to our estimates the light fluxes in measurements with two readout systems coincide with an accuracy of ±5%. It can be seen that the counting rates in the regions of the hollow and the maximum in the single-electron spectrum approximately coincide.

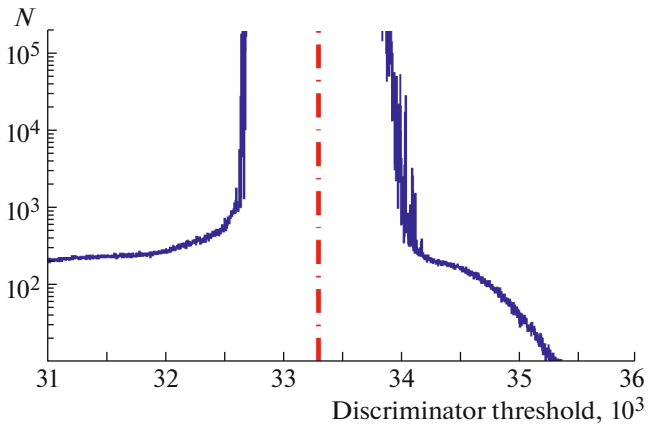

Fig. 16. The dependence of the front-recording rate on the detection threshold in the range including the baseline (the dashed–dotted line).

The ratio of the amplitudes corresponding to the maximum and the hollow is 2.6 in both cases. In the case of the PADIWA board, on the one hand, the hollow is more pronounced, and on the other, there is an excess of counts at small amplitudes, which implies a greater relative contribution of interference and, therefore, the impossibility of separating the low-amplitude part of the one-electron spectrum from them and the inexpediency of increasing the efficiency by setting the threshold below the hollow.

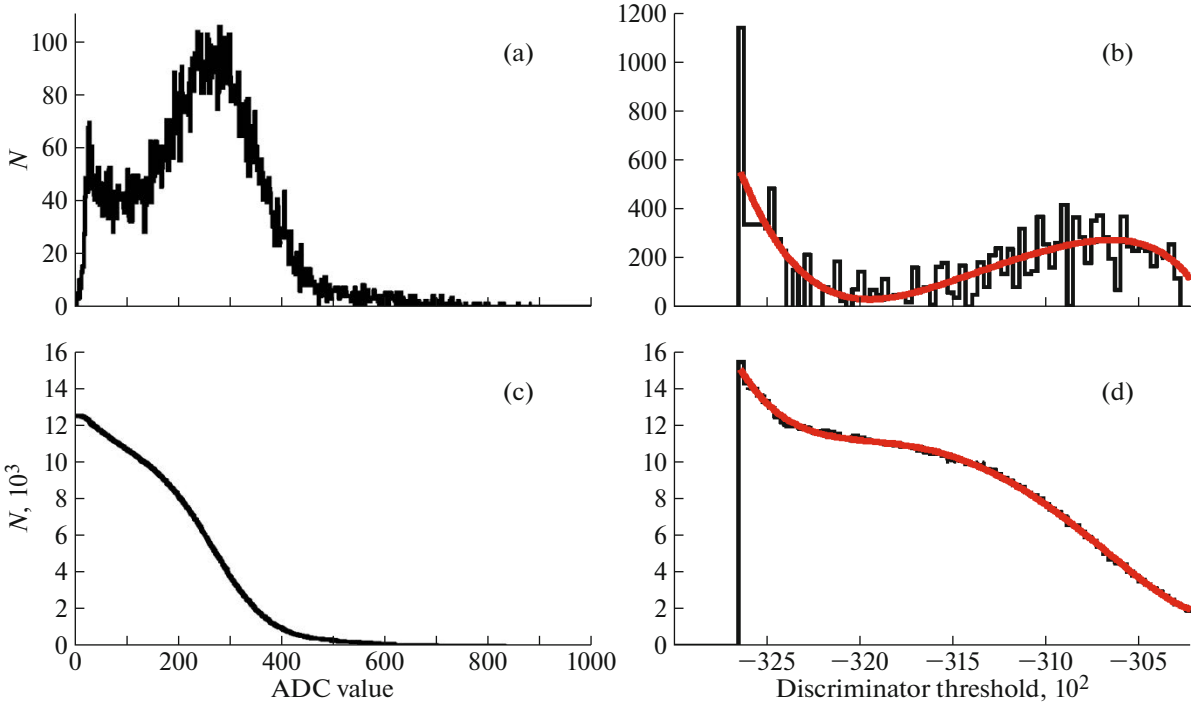

Fig. 17. (a) The single-electron spectrum measured directly with the help of the n-XYTER readout system, (b) the threshold scan derived from the readout system based on the PADIWA and TRB v3 boards, (c) the integral of the single-electron spectrum, and (d) the dependence of the counting rate on the discriminator threshold.

7. CONCLUSIONS

The properties of the prototype of the readout and data-acquisition system of the RICH detector for the CBM experiment have been investigated. The 64-channel module that consists of H12700 MAPMTs, four PADIWA preamplifier boards, and one TRB v3 board and performs the functions of the TDC and data concentrator is described in detail. The software modules necessary for operation of the prototype are described. The procedure for calibrating inter-channel delays and the stability of obtained delays are considered. The drift of individual delays does not exceed 0.5 ns for the entire measurement time.

The possibility of using the "time over threshold" (ToT) spectra for selecting correct hits and correcting the time reference is considered. It is revealed that the ToT spectrum has a multi-peak structure due to periodic noise pickups. This prevents the use of this parameter in the analysis. The detected circuitry faults will be eliminated in the next version of the readout electronics boards.

The time properties of the WLS and its effect on the detection efficiency for Cherenkov rings are investigated. The most-intense fast component is characterized by a decay time of 1.1 ns; nevertheless, there are also components with characteristic times of 3.8 and 45 ns. Comparison is made between the slow analog and the fast timing readouts of the MAPMT are compared.

It has been revealed that the features in the single-electron spectrum are displayed in the way in which the photoelectron detection efficiency and the probability of the appearance of false hits depend on the discriminator threshold. The time resolution of the entire readout channel for different sets of channels (from one pair to 131) has been studied. The worst value obtained is 1.1 ns (FWHM), which is primarily determined by the absence of timestamp correction depending on the signal amplitude and the drift of the inter-channel delays. The results obtained are sufficient to using the investigated system of readout and data acquisition in the CBM experiment, but the elimination of the identified shortcomings will help to create the efficiency margin and increase the reliability of the system in long-term operation.

REFERENCES

1. Gutbrod, H.H., *FAIR Baseline Technical Report*, ISBN: 3-9811298-0-6, 2006.
2. *The CBM Physics Book: Compressed Baryonic Matter in Laboratory Experiments,* Friman B. et al., Eds., Berlin, Springer-Verlag, 2011, in Ser.: *Lecture Notes in Physics,* vol. 814. doi 10.1007/978-3-642-13293-3
3. The CBM Collaboration, *Nuclear Matter Physics at SIS-100, CBM Report 2012-01*, Senger, P. and Friese, V., Eds., Darmstadt: GSI, 2012.
4. *Compressed Baryonic Matter Experiment. Technical Status Report*, Darmstadt: GSI, 2005.
5. *CBM Progress Report 2016,* Selyuzhenkov, I. and Toia, A., Eds., Darmstadt: GSI, 2017, GSI-2017-00564.
6. *Technical Design Report for the CBM Superconducting Dipole Magnet*, Malakhov, A. and Shabunov, A., Eds., Darmstadt: GSI, 2013, GSI-2015-02000.
7. Koziel, M., Amar-Youcef, S., Bialas, N., Deveaux, M., Fröhlich, I., Li, Q., Michel, J., Milanović, B., Müntz, C., Neumann, B., Schrader, C., Stroth, J., Tischler, T., Weirich, R., and Wiebusch, M., *Nucl. Instrum. Methods Phys. Res., Sect. A*, 2013, vol. 732, p. 515. doi 10.1016/j.nima.2013.07.041
8. *Technical Design Report for the CBM Silicon Tracking System (STS),* Heuser, J., et al., Eds., Darmstadt: GSI, 2013, GSI-2013-05499.
9. *Technical Design Report for the CBM Ring Imaging Cherenkov Detector (RICH),* Höhne, C., Ed., Darmstadt: GSI, 2013, GSI-2014-00528.
10. *Technical Design Report for the CBM: Muon Chambers (MuCh)*, Chattopadhyay, S., et al., Eds., Darmstadt: GSI, 2015, GSI-2015-02580.
11. Biswas, S., Schmidt, D.J., Abuhoza, A., Frankenfeld, U., Garabatos, C., Hehner, J., Kleipa, V., Morhardt, T., Schmidt, C.J., Schmidt, H.R., and Wiehula, J., *J. Instrum,* 2013, vol. 8, p. C12002. doi 10.1088/1748-0221/8/12/C12002
12. Petris, M., Petrovici, M., Catanescu, V., Tarzila, M., Simion, V., Bartos, D., Berceanu, I., Bercuci, A., Caragheorgheopol, G., Constantin, F., Radulescu, L., Adamczewski-Musch, J., and Linev, S., *Nucl. Instrum. Methods Phys. Res., Sect. A*, 2013. vol. 732. p. 375. doi 10.1016/j.nima.2013.07.087
13. *Technical Design Report for the CBM Time-of-Flight System (TOF)*, Herrmann, N., Ed., Darmstadt: GSI, 2014, GSI-2015-01999.
14. Korolko, I.E., Prokudin, M.S., and Zaitsev, Yu.M., *J. Phys.: Conf. Ser.*, 2017, vol. 798, p. 012164. doi 10.1088/1742-6596/798/1/012164
15. *Technical Design Report for the CBM Projectile Spectator Detector (PSD),* Guber, F. and Selyuzhenkov, I., Eds., Darmstadt: GSI, 2015, GSI-2015-02020.
16. *Hamamatsu H12700 Manual.* https://www.hamamatsu.com/resources/pdf/etd/H12700_TPMH1348E.pdf.
17. Calvi, M., Carniti, P., Cassina, L., Gotti, C., Maino, M., Matteuzzi, C., and Pessina, G., *J. Instrum.*, 2015, vol. 10, p. 09021. doi 10.1088/1748-0221/10/09/P09021
18. https://www.hamamatsu.com/resources/pdf/etd/H8500_H10966_TPMH1327E.pdf.
19. Adamczewski-Musch, J., Akishin, P., Becker, K.-H., Belogurov, S., Bendarouach, J., Boldyreva, N., Chernogorov, A., Deveaux, C., Dobyrn, V., Dürr, M., Eschke, J., Förtsch, J., Heep, J., Höhne, C., Kampert, K.-H., et al., *Nucl. Instrum. Methods Phys. Res., Sect. A,* 2017, vol. 845, p. 434. doi 10.1016/j.nima.2016.05.102
20. Adamczewski-Musch, J., Akishin, P., Becker, K.-H., Belogurov, S., Bendarouach, J., Boldyreva, N., Chernogorov, A., Deveaux, C., Dobyrn, V., Dürr, M., Eschke, J., Förtsch, J., Heep, J., Höhne, C., Kampert, K.-H., et al., *J. Instrum.*, 2016, vol. 11, C05016. doi 10.1088/1748-0221/11/05/C05016
21. *Photomultiplier Tubes. Basics and Applications,* Hamamatsu Photonics K.K.

22. Kopfer, J., *PhD Thesis*, Wuppertal, Bergische Univ. Wuppertal, 2014.
23. Official TRB Project Web Site. http://trb.gsi.de/.
24. Ugur, C., Linev, S., Michel, J., Schweitzer, T., and Traxler, M., *J. Instrum.*, 2016, vol. 11, C01046. doi 10.1088/1748-0221/11/01/C01046
25. *TRB v3 Documentation*. http://jspc29.x-matter.uni-frankfurt.de/docu/trb3docu.pdf.
26. Zabołotny, W.M. and Kasprowicz, G., *Photonics Applications in Astronomy, Communications, Industry, and High-Energy Physics Experiments*, 2014, vol. 929023. doi 10.1117/12.2073377
27. de Cuveland, J. and Lindenstruth, V. (for the CBM Collaboration), *J. Phys.: Conf. Ser.*, 2011, vol. 331, p. 022006. doi 10.1088/1742-6596/331/2/022006
28. Michel, J., Faul, M., Friese, J., Höhne, C., Kampert, K.-H., Patel, V., Pauly, C., Pfeifer, D., Skott, P., Traxler, M., and Ugur, C., *J. Instrum.*, 2017, vol. 12, C01072. doi 10.1088/1748-0221/12/01/C01072
29. Adamczewski-Musch, J., Kurz, N., Linev, S., and Zumbruch, P., *J. Phys.: Conf. Ser*, 2012, vol. 396, p. 012001. doi 10.1088/1742-6596/396/1/012001
30. Bergmann, C., Emschermann, D., Amend, W., Bercuci, A., Berendes, R., Blume, C., Dillenseger, P., Garcia, C., Gläßel, S., Heine, N., Hutter, D., Kardan, B., Kohn, M., Krieger, M., Morhardt, T., et al., in *CBM Progress Report 2014*, Darmstadt: GSI, 2014, p. 9.
31. Bergmann, C., Emschermann, D., Berendes, R., Heine, N., Kohn, M., Verhoeven, W., and Wessels, J.P., in *CBM Progress Report 2014*, Darmstadt: GSI, 2014, p. 78.
32. Petris, M., Batros, D., Caragheorghropol, G., Constantin, F., Petrovici, M., Radulescu, L., Simion, V., Deppner, I., Herrmann, N., Simon, C., Fruehauf, J., Kis, M., and Loizeau, P-A., *J. Phys.: Conf. Ser*, 2016, vol. 724, p. 012037. doi 10.1088/1742-6596/724/1/012037
33. *Information About the T9 Beam Line and Experimental Facilities*. http://home.web.cern.ch/sites/home.web.cern.ch/files/file/spotlight_students/information_about_the_t9_ beam_line_and_experimental_facilities.pdf.
34. Kotchenda, L.M. and Kravtsov, P.A., *CBM RICH Prototype Gas System,* http://hepd.pnpi.spb.ru/hepd/articles/6.pdf.
35. Adamczewski-Musch, J., Becker, K.-H., Belogurov, S., Boldyreva, N., Chernogorov, A., Deveaux, C., Dobyrn, V., Dürr, M., Eom, J., Eschke, J., Höhne, C., Kampert, K.-H., Kleipa, V., Kochenda, L., Kolb, B., et al., *Nucl. Instrum. Methods Phys. Res., Sect. A*, 2014, vol. 766, p. 221. doi 10.1016/j.nima.2014.04.074
36. Bendarouach, J., Höhne, C., and Mahmoud, T., in *CBM Progress Report 2014*, Darmstadt: GSI, 2014, p. 56.
37. *Roithner UVTOP240 Datasheet*. http://www.roithner-laser.com/datasheets/led_deepuv/uvtop240.pdf.
38. Adamczewski-Musch, J., Becker, K.-H., Belogurov, S., Boldyreva, N., Chernogorov, A., Deveaux, C., Dobyrn, V., Dürr, M., Eom, J., Eschke, J., Höhne, C., Kampert, K.-H., Kleipa, V., Kochenda, L., Kolb, B., et al., *Nucl. Instrum. Methods Phys. Res., Sect. A*, 2015, vol. 783, p. 43. doi 10.1016/j.nima.2015.02.014
39. *Alphalas Picopower-LD Series Datasheet*. http://www.alphalas.com/images/stories/products/lasers/Picosecond_Pulse_Diode_Lasers_with_Driver_PICOPOWER-LD_ALPHALAS.pdf
40. http://www.rz.uni-frankfurt.de/39888789/syscore.
41. http://cbmroot.gsi.de/.
42. FLESnet Development Repository. https://github.com/cbm-fles/flesnet.
43. Adamczewski-Musch, J., Linev, S., Ovcharenko, E., and Ugur, C., *HADES trbnet Data Formats for DABC and Go4: GSI Scientific Report 2012*, Darmstadt: GSI, 2013, PHN-SIS18-ACC-41, p. 297.
44. Szplet, R., Kalisz, J., and Pelka, R., *IEEE Trans. Instrum. Meas.*, 1997, vol. 46, p. 449.
45. Adamczewski-Musch, J., Akishin, P., Becker, K.-H., Belogurov, S., Bendarouach, J., Boldyreva, N., Deveaux, C., Dobyrn, V., Dürr, M., Eschke, J., Förtsch, J., Heep, J., Höhne, C., Kampert, K.-H., Khanzadeev, A., et al., *Phys. Part. Nucl. Lett.*, 2017, vol. 14, no. 6, p. 904. doi 10.1134/S1547477117060036
46. Adamczewski-Musch J., Akishin P., Becker K.-H., Belogurov S., Bendarouach J., Boldyreva N., Deveaux C., Dobyrn V., Dürr M., Eschke J., Förtsch J., Heep J., Höhne C., Kampert K.-H., Khanzadeev A., et al., *Nucl. Instrum. Methods Phys. Res., Sect. A*, 2017, vol. 846, p. 246. doi 10.1016/j.nima.2017.03.043
47. Lebedev, S.A. and Ososkov, G.A., *Phys. Part. Nucl. Lett.*, 2009, vol. 6, no. 2, p. 161.
48. Lebedev, S., Höhne, C., Kisel, I., and Ososkov, G., *Fast Parallel Ring Recognition Algorithm in the RICH Detector of the CBM Experiment at FAIR*, Dubna: Ob'edin. Inst. Yad. Issled., 2011, PoS(ACAT2010)060.
49. O'Connor, D.V., *Time-correlated Single Photon Counting,* London: Academic, 1984.
50. Gonnella, F., Kozhuharov, V., and Raggi, M., *Nucl. Instrum. Methods Phys. Res., Sect. A*, 2015, vol. 791, p. 16. doi 10.1016/j.nima.2015.04.028

Translated by N. Goryacheva